

# Real-time whole-brain imaging of hemodynamics and oxygenation at micro-vessel resolution with ultrafast wide-field photoacoustic microscopy

Junjie Yao (✉ [junjie.yao@duke.edu](mailto:junjie.yao@duke.edu))

Duke University <https://orcid.org/0000-0002-2381-706X>

Xiaoyi Zhu

Duke University

Qiang Huang

Duke University

Anthony DiSpirito

Duke University

Tri Vu

University at Buffalo

Qiangzhou Rong

Duke University <https://orcid.org/0000-0002-7549-9278>

Xiaorui Peng

Duke University

Huaxin Sheng

Duke University

Xiling Shen

Duke University

Qifa Zhou

University of Southern California

Laiming Jiang

University of Southern California

Ulrike Hoffmann

Duke University

---

## Article

**Keywords:** High-speed whole-brain imaging, brain hemodynamics, photoacoustic microscopy, widefield imaging, blood oxygenation, hypoxia, stroke, spreading depolarization wave

**Posted Date:** January 13th, 2022

**DOI:** <https://doi.org/10.21203/rs.3.rs-1230249/v1>

**License:**  This work is licensed under a Creative Commons Attribution 4.0 International License.

[Read Full License](#)

---

**Version of Record:** A version of this preprint was published at Light: Science & Applications on May 17th, 2022. See the published version at <https://doi.org/10.1038/s41377-022-00836-2>.

# Real-time whole-brain imaging of hemodynamics and oxygenation at micro-vessel resolution with ultrafast wide-field photoacoustic microscopy

Xiaoyi Zhu<sup>1</sup>, Qiang Huang<sup>1</sup>, Anthony DiSpirito<sup>1</sup>, Tri Vu<sup>1</sup>, Qiangzhou Rong<sup>1</sup>, Xiaorui Peng<sup>1</sup>, Huaxin Sheng<sup>3</sup>, Xiling Shen<sup>1</sup>, Qifa Zhou<sup>2,3</sup>, Laiming Jiang<sup>2,3,\*</sup>, Ulrike Hoffmann<sup>4,\*</sup>, Junjie Yao<sup>1,\*</sup>

<sup>1</sup> Department of Biomedical Engineering, Duke University, Durham, NC 27708, USA

<sup>2</sup> Department of Biomedical Engineering, University of Southern California, Los Angeles, CA 90089, USA

<sup>3</sup> Roski Eye Institute, Department of Ophthalmology, Keck School of Medicine, University of Southern California, Los Angeles, California 90033, USA.

<sup>4</sup> Department of Anesthesiology, Duke University, Durham, NC 27708, USA

\*Correspondence: [laiming\\_jiang@foxmail.com](mailto:laiming_jiang@foxmail.com); [ulrike.hoffmann@duke.edu](mailto:ulrike.hoffmann@duke.edu); [junjie.yao@duke.edu](mailto:junjie.yao@duke.edu);

## Abstract

High-speed high-resolution imaging of the whole-brain hemodynamics is urgently needed to facilitate the next level of neurovascular research. Image acquisition speed and image quality are crucial to visualizing real-time hemodynamics in complex brain vascular networks, and displaying fast pathophysiological dynamics on a micro and macro-level, enabling advances in current queries in neurovascular and brain metabolism research, including stroke, dementia and acute brain injury. Further, real-time oxygen saturation of hemoglobin (sO<sub>2</sub>) imaging to differentiate arteries from veins and capture fast-paced oxygen delivery dynamics is needed to solve pertinent questions in these fields and beyond. Here, we present a novel ultrafast functional photoacoustic microscopy (UFF-PAM) to image the whole-brain hemodynamics and oxygen delivery. UFF-PAM takes advantage of several key engineering innovations, including Raman-shifter-based dual-wavelength laser excitation, water-immersible 12-facet-polygon scanner, high-sensitivity ultrasound transducer, and deep-learning-based image upsampling. A volumetric imaging rate of 2 Hz has been achieved over a field of view (FOV) of 11 × 7.5 × 1.5 mm<sup>3</sup> with a

high spatial resolution of  $\sim 10 \mu\text{m}$ . Using the UFF-PAM system, we have demonstrated proof-of-concept functional studies on the mouse brains in response to systemic hypoxia, sodium nitroprusside, and stroke. We observed the mouse brain's fast morphological and functional changes over the entire cortex, including vasoconstriction, vasodilation, and deoxygenation. More interestingly, for the first time, under the whole-brain FOV and micro-vessel resolution, we captured the vasoconstriction and oxygenation change simultaneously in the spreading depolarization (SD) wave. Our work provides a great potential for fundamental brain research under various pathological and physiological conditions.

### **Keywords**

High-speed whole-brain imaging, brain hemodynamics, photoacoustic microscopy, widefield imaging, blood oxygenation, hypoxia, stroke, spreading depolarization wave

### **INTRODUCTION**

Imaging technologies capable of visualizing real-time hemodynamics in complex brain vascular networks, on a micro and macro-level, are urgently needed to facilitate the understanding of current queries in neurovascular and brain metabolism research, including but not limited to stroke, dementia and management of acute brain injury [1, 2]. Further, additional features, like real-time oxygen saturation of hemoglobin ( $s\text{O}_2$ ) imaging, essential for the distinction of arteries and veins, are needed to capture fast-paced oxygen delivery dynamics and ultimately brain metabolism. However, advances in these fields have been hampered by the fact that existing brain imaging technologies suffer various limitations, particularly lacking imaging speed and image resolution as well as compromising the field of view (FOV).

While positron emission tomography (PET) and functional magnetic resonance imaging (fMRI) can provide excellent penetration, they suffer from low spatial and temporal resolutions. Optical microscopy is widely used for studying brain functions with high resolution, but it is often hampered by slow imaging speed [3] or poor penetration depth [4]. Microbubble-enhanced ultrasound imaging has been used for brain research with deep penetration and high resolution, but it still lacks functional sensitivity [5].

The emerging photoacoustic microscopy (PAM), which detects ultrasound signals induced by optical absorption [6, 7], has demonstrated increasing impact in brain studies. Particularly, PAM

is capable of functional and molecular imaging with various endogenous and exogenous contrasts, such as measuring the blood oxygenation, blood flow, and metabolic rate of oxygen. However, like other scanning-based imaging technologies, it remains a technical challenge for PAM to achieve high imaging speed, large field of view (FOV), high spatial resolution, and high detection sensitivity simultaneously.

While traditional PAM systems use slow motor scanning [8, 9], recent advances in high-speed PAM have explored faster scanning mechanisms, including galvo scanners [10-12], water-immersible microelectromechanical systems (MEMS) scanners [13-17], and polygon scanning systems [18, 19]. Among them, the polygon scanner can provide repeated line scanning over a large scanning range with simple rotary driving [20-22]. The polygon scanner is advantageous over the galvo scanner and MEMS scanner, because its scanning range does not depend on the scanning frequency. Previously, we reported the first implementation of a high-speed PAM system based on a 6-facet polygon scanner [23] that achieved a 900 Hz line scanning rate over a 12-mm scanning range, which was a thousand times faster than traditional motor-based PAM systems. However, the previous polygon PAM was not capable of functional brain imaging with a single-wavelength excitation. Moreover, because of the limited laser pulse repetition rate, the image quality was severely compromised due to spatial undersampling at high imaging speed.

Here, we present an ultrafast functional photoacoustic microscopy (UFF-PAM), which enables the imaging of whole-brain microvasculature and functional dynamics in response to physiological and pathophysiological challenges, with a wide FOV and high spatial resolution. We have developed a diamond-ground metal polygon with 12 facets, driven by a water-immersible high-speed DC motor, which can steer the confocal beam of laser excitation and ultrasound detection simultaneously. Its maximum line scanning rate is more than 2 kHz over an 11 mm scanning range, which is more than two times faster than the previously reported polygon PAM systems [23, 24]. More importantly, we have developed a simulated Raman shifter to provide dual-wavelength excitation at 532 nm and 558 nm, enabling functional brain imaging at high speed. We have developed an automatic image registration method to overcome the misalignment of the polygon facets due to water damping. Moreover, we have applied a deep learning approach to mitigate the spatial undersampling and substantially improved the image quality.

As proof-of-concept, we have demonstrated UFF-PAM of hemodynamic responses in mouse brains to hypoxia, sodium nitroprusside (SNP) induced systemic hypotension, and ischemic stroke. For hypoxia challenge, UFF-PAM monitored the global hemoglobin deoxygenation in the brain and the resultant vasodilation. For the SNP challenge, UFF-PAM imaged the progress of arterial dilation and the resultant blood oxygenation dynamics. For the ischemic stroke, UFF-PAM captured the functional response of brain microvasculature during and post the stroke, particularly, the stroke-induced spreading depolarization (SD) waves. Enabled by the large FOV and high imaging speed, UFF-PAM can precisely pinpoint the SD wave's originating position, and track its propagation direction and spreading pattern. With high spatial resolution, UFF-PAM can clearly resolve the local vasoconstriction and deoxygenation associated with the SD waves on the single-vessel level. All in all, with its unique capability of capturing fast hemodynamics, UFF-PAM may become a powerful tool to address a multitude of important questions in functional brain research.

## RESULTS

### The UFF-PAM system

**Figure 1a** illustrates the schematic of the UFF-PAM system. Two lasers are used for the dual-wavelength PA excitation (**Supplementary Fig. 1a**). One laser (VPFL-G-20, Spectral-Physics) generates the 532 nm light beam, and the other laser (SPFL-532-40, Spectral-Physics) is used for the 558 nm Raman path. A half-wave plate (AHWP05M-580, Thorlabs) adjusts the polarization state of the Raman pump beam to achieve a high Raman shift efficiency. The Raman pump beam is focused by an objective (UPLFLN 20×, Olympus) and then coupled into a 6.5-meter-long polarization maintenance fiber (HB450-SC, FIBERCORE) to generate the 558 nm light (**Supplementary Fig. 1b**). The conversion efficiency of the Raman path is about 33% at 558 nm (**Fig. 1b**). A dichroic mirror (DMSP550, Thorlabs) combines the 532 nm beam and the 558 nm beam. The combined laser beam is focused by an objective lens (ACN127-050-A, Thorlabs) through the central aperture of a spherically-focused ring-shaped ultrasound transducer (central frequency, 40 MHz; bandwidth, 100%; focal length, 14 mm). The optical beam spot size on the sample surface is ~10 μm. Both the excitation laser beam and the resultant PA waves are steered by a lab-made water-immersible 12-facet polygon scanner, with confocal alignment across the fast scanning range (**Supplementary Video 1**). The PA signal is amplified and sampled at 250 MHz

(ATS9350, Alarzar Tech). The laser firing, polygon scanning, stepper motor motion, and data sampling are all synchronized by an FPGA system (myRIO, National Instruments).

In UFF-PAM, the relative concentrations of oxy-hemoglobin (HbO<sub>2</sub>) and deoxy-hemoglobin (HbR) are quantified from the PA signals generated by the pair of laser pulses at 532 nm and 558 nm (**Fig. 1c**). A linear unmixing method is used to compute the oxygen saturation of hemoglobin (sO<sub>2</sub>). A lab-made start of scan (SOS) detection system uses a multi-mode fiber to detect the starting position of the scanning laser beam by each facet (**Fig. 1d, Supplementary Fig. 1c**). While each laser pulse generates one-dimensional time-resolved PA signal, volumetric imaging is achieved by fast polygon scanning along the *x*-axis (fast axis) and stepper motor scanning along the *y*-axis (slow axis) (**Fig. 1e**). The SOS signal is used to synchronize the fast-axis polygon scanning with the slow-axis stepper motor scanning. Both the vascular structure and the oxygenation map can be obtained by a single scan with dual-wavelength excitation. No optical wavelength switching is needed. We have developed a longitudinal whole-cortex cranial window that is both optically and acoustically transparent for PA imaging (see **Methods**). The cranial window can effectively improve the resolution and signal to noise ratio of the PA images, by eliminating the skull's optical scattering and acoustic attenuation.

**Figures 1f-g** are the representative mouse brain images acquired by UFF-PAM, showing the whole-cortex vasculature network and vessel-by-vessel sO<sub>2</sub> map, respectively. UFF-PAM can achieve a maximum time-resolved 1D frame rate of 2 MHz, an *x-z* 2D frame rate of 2 kHz over 11 × 1.5 mm<sup>3</sup>, and a 3D frame rate of 2 Hz over an 11 × 7.5 × 1.5 mm<sup>3</sup> FOV (**Supplementary Fig. 2**), which is 3600 times faster than the traditional slow-scanning PAM system and sufficient to cover the entire cortex of an adult mouse brain. The imaging speed of UFF-PAM can be adjusted based on the laser pulse repetition rate (PRR) and the desired spatial sampling density (or scanning step size). With rotational scanning, the effective scanning step size along the fast axis is not uniform on the sample surface, with an increasing scanning step size towards the two ends of the scanning range (**Supplementary Fig. 3a**). Additionally, limited by the laser PRR, there is a tradeoff between the 2D frame rate and the scanning step size. Because the polygon scanner generates a curved in-focus scanning trajectory, the detection sensitivity and spatial resolution over the scanning range is not uniform, which is the highest in the middle and lowest on both ends (**Supplementary Figs. 3b**). The lateral resolution ranges from 7 μm to 18 μm over the scanning

range (**Supplementary Figs. 3c-d**). Unlike the lateral resolution, the axial resolution of the UFF-PAM system is determined by the detected ultrasound bandwidth [32], which is  $\sim 33 \mu\text{m}$  across the scanning range. For *in vivo* experiments, we usually reduce the volumetric frame rate to 0.3 Hz, with a PRR of 800 kHz, a 2D frame rate of 1 kHz, and a scanning step size of 15–19  $\mu\text{m}$ . Note that the relatively large scanning step size leads to severe spatial undersampling which will be addressed below.

### **Facet registration and deep learning based upsampling**

**Figure 2a** illustrates the data processing procedure in UFF-PAM, which includes facet registration, deep learning based upsampling, and frame stabilization. Because the polygon scanner is fully immersed in water for acoustic coupling, the water damping force induces wobbling motion of the polygon. Moreover, the twelve facets have minor variations in their dimensions. Together, there exists misalignment among the scanning trajectory of different facets, resulting in discontinuous and distorted images (**Figs. 2b and 2c**). Although each facet can provide self-consistent scanning (**Fig. 2d**), the large scanning step size and undersampling lead to poor image quality. To mitigate the scanning misalignment due to polygon wobbling and facet variation, we have developed a geometric-transformation registration method to find the difference between each facet and subsequently realign the images (see **Methods**). With image registration from all twelve facets, the misaligned image can be substantially improved with more continuous vessels (**Fig. 2e**).

However, even with the facets aligned, UFF-PAM still suffers from the undersampling due to the large scanning step size. The undersampling results in discontinuous vessel boundaries and pixelized vessel lumen (**Fig. 2e**). To address the undersampling, we have developed a deep-learning-based upsampling strategy, adapted from our previous modified Fully Dense U-net (FD U-net) model upsampling pipeline (**Supplementary Figs. 4 and 5**; also see **Methods**) [25]. We trained the upsampling model using fully-sampled brain vasculature images to maintain vessel continuity, and used the trained model to restore the undersampled PAM images (**Supplementary Fig. 4b**). Compared with the undersampled image in **Fig. 2e**, the upsampled result in **Fig. 2f** shows smoother vessel boundaries, reduced undersampling artifacts, and more consistent vessel intensity and vessel profile (**Fig. 2g**). We also compared the deep learning based upsampled result with bicubic interpolation (**Supplementary Fig. 6**). Bicubic interpolation created images with blurring,

jagged and discontinuous vessel profiles, and failed to improve the image quality. The facet alignment and image upsampling are critical steps to restore the vessel structures in UFF-PAM, providing better vessel fidelity for further quantitative analysis (**Figs. 2h-k**).

### ***In vivo* high-speed functional imaging of cerebral hemodynamics by UFF-PAM**

Imaging hemodynamics in the mouse brain in particular at the microvessel level is highly desired for understanding neurovascular coupling and the regulation of cerebral blood flow in both healthy and diseased states. To demonstrate UFF-PAM's high speed and large FOV, we captured cerebral hemodynamic responses to three pathophysiological challenges: 1) systemic hypoxia, 2) systemic vasodilation with sodium nitroprusside (SNP), and 3) ischemia-triggered cortical spreading depolarization waves and spreading ischemia. The imaging parameters are summarized in **Supplementary Table 1** and **Table 2**.

#### ***Systemic hypoxia challenge***

To demonstrate UFF-PAM's performance in capturing fast hemodynamic responses in the brain, we applied systemic hypoxia to the animals by decreasing the inspiratory oxygen content from 21% (normoxia) to 3% (hypoxia). After baseline imaging under normoxia, we introduced hypoxia for 2 minutes and imaged the resultant hemodynamic changes in the brain vasculature. We repeated the normoxia-hypoxia cycle three times. At normoxia, the UFF-PAM images can clearly differentiate arteries and veins, based on their sO<sub>2</sub> levels (**Figs. 3a** and **3d**; **Supplementary Videos 2** and **3**). Upon the hypoxia challenge, we observed an immediate decrease in sO<sub>2</sub> levels in both arteries and veins across the brain (**Figs. 3b** and **3e**). By analyzing the arterial and venous vessels separately, we were able to depict their different changes in sO<sub>2</sub>, an important capability provided by the single-vessel resolution of UFF-PAM. As expected, the averaged sO<sub>2</sub> level in veins decreased by 85±2% ( $p<0.001$ ), while sO<sub>2</sub> in arteries decreased by 70±2% ( $p<0.001$ ), as shown in **Fig. 3g**. The reduction and recovery of sO<sub>2</sub> levels were reproducible. Moreover, hypoxia induced significant vasodilation (**Fig. 3h**). Representative arteries dilated by 3% ( $p<0.001$ ), representative veins dilated by 4.5% ( $p<0.001$ ). By analyzing all vessels over the entire cortex, we found a clear increase in the total vessel area in the brain (**Fig. 3i**), confirming a well-documented phenomenon in humans [26-29]. Continuous PA imaging over a 30-min period further showed a gradual decrease in the baseline sO<sub>2</sub> level even under the normoxia condition, likely due to the increase in

oxygen extraction fraction (OEF) induced by the repeated hypoxia challenge, which was consistent with previous studies on humans under hypoxic conditions [30-32].

### ***Systemic vasodilation and vasoconstriction induced by sodium nitroprusside***

While the hypoxia experiment focused on physiological challenge induced hemodynamic changes, the sodium nitroprusside (SNP) experiment aimed to investigate fast brain hemodynamics in response to a systemic hypotension. SNP is commonly used in clinical practice to dilate arteries and veins in order to ameliorate hypertension and reduce cardiac afterload [33-36]. We used UFF-PAM to detect fast hemodynamic changes induced by systemic SNP administration (**Supplementary Videos 4 and 5**). After monitoring the brain for 5 mins as the baseline (**Figs. 4a and 4e**), a single dose of SNP was infused via a femoral vein catheter over 40 seconds. We continuously monitored the hemodynamic response in the brain for 35 minutes. As expected, SNP induced substantial vasodilation and thus decrease in systemic blood pressure from 80 mmHg to 30 mmHg, measured by an intravascular pressure sensor (**Supplementary Fig. 7**). UFF-PAM observed the vasodilation process in the brain, which peaked at 2.5 minutes in major arteries and veins after the SPN infusion, with an  $18\pm 2\%$  ( $p < 0.001$ ) increase in the vessel diameters (**Figs. 4b and 4f**). Vasodilation was more pronounced in major arteries ( $19\pm 5\%$ ) than in major veins ( $15\pm 2\%$ ) (**Fig. 4i**). Consistent with SNP's short effective duration, the venous dilation gradually subsided after about 5 minutes, while the arterial dilation persisted longer.

Counter intuitively, we also observed clear vasoconstriction in many microvessels (**Figs. 4e and 4f**). In fact, the vasoconstriction of the microvessels outweighed the vasodilation of the major vessels, and thus the total vessel area decreased by as much as  $\sim 5\%$  (**Fig. 4j**). We believe that the SNP-induced decrease in the systemic blood pressure (**Supplementary Fig. 7**) constitutes the major reason for the observed microvascular constriction. Overall, SNP caused stronger cerebral vessel dilation than systemic hypoxia, especially in the arteries, consistent with its pharmacological profile and clinical use [36]. Drastically different responses to SNP in various vessel types highlighted the value of large FOV and high resolution of UFF-PAM.

We further observed significant deoxygenation of hemoglobin after SNP administration. The venous  $sO_2$  decrease ( $65\pm 10\%$ ,  $p < 0.001$ ) was much larger than the arterial  $sO_2$  decrease ( $38\pm 4\%$ ,  $p < 0.001$ ), within 2.5 minutes after the SNP administration (**Fig. 4k**). The different arterial and venous responses may reflect that SNP affected both oxygen delivery and consumption. Further,

as shown in **Supplementary Fig. 7**, brain tissue oxygenation decreased substantially in tandem with the decrease in systemic blood pressure. Similar to the microvessel constriction in the brain, the constricted microvessels in the lung tissues might reduce the gas exchange efficiency and thus lead to the decrease in the arterial sO<sub>2</sub> [37, 38]. Reduced capillary perfusion resulted in a higher oxygen extraction fraction (OEF), which contributed to the lower sO<sub>2</sub> in the collecting veins (*i.e.*, higher oxygen consumption) and decrease in tissue oxygenation. [35]. Overall, with its high speed, large FOV, and high resolution, UFF-PAM not only confirmed the expected global vasodilation induced by SNP, but also observed the vasoconstriction in microvessels and global deoxygenation.

### ***Stroke-induced cortical spreading ischemia***

Spreading depolarization (SD) waves are intense neuronal and glial depolarization waves that propagate at a speed of millimeters/minute in the gray matter, and are associated with massive transmembrane ion and water transportation, elevated extracellular excitatory amino acid levels, and a heavy metabolic burden to homeostasis [39, 40]. Recurring SD waves can originate from the ischemic tissue in a spontaneous and random manner, and propagate throughout the vulnerable hemisphere [41, 42]. The peri-infarct SD waves can exacerbate ischemic injury by imposing additional metabolic burden with vasoconstriction, also termed spreading ischemia [40, 43, 44]. In addition, it has recently been reported that the lack of oxygen supply in the brain tissue can trigger SD waves [45]. In this experiment, we aimed to study the propagating cortical SD waves and the associated hemodynamics at the microvessel level. To do so, we performed a permanent stroke procedure on the left hemisphere by completely occluding the left carotid artery (**Supplementary Fig. 8**). We also temporarily occluded the right carotid artery to increase the ischemic burden and reduce the collateral blood supply through the circle of Willis. We used UFF-PAM to monitor the cortical vasculature and hemoglobin oxygenation changes throughout the entire procedure (**Supplementary Fig. 9; Supplementary Videos 6 and 7**).

After ~9 minutes of bilateral carotid artery occlusion, we observed five spontaneous SD waves in the permanently occluded left hemisphere (**Supplementary Videos 8 and 9**). There are several important observations by UFF-PAM enabled by its large FOV, high speed, and high resolution. (1) By tracking the wave propagation over time across the left hemisphere, we were able to calculate the average SD wave speed as  $2.56 \pm 0.23$  mm/min, which was consistent with previous reports [46-48]. (2) We were able to precisely localize the originating point of each SD wave (**Figs.**

**5b-c; Supplementary Video 10**), and map the spreading direction, pattern, duration, and affected area (**Fig. 5d**). This information was critical in mapping the core and penumbra areas in the cerebral stroke. (3) We were able to quantify the local vasoconstriction along the propagation path of an SD wave (**Figs. 5e, 5g and 5i**), which were followed by the decrease of local sO<sub>2</sub> (**Figs. 5f, 5h and 5j**). Our results confirmed that, along the SD wave path, the local oxygen demand of the peri-infarct tissue could not be matched by the compensatory increase in local blood supply, leading to an increase in the oxygen extraction fraction. As a result, our results have clearly shown that the SD waves were essentially spreading waves of vasoconstriction, accompanied by spreading waves of hypoxia, which effectively demonstrated the spreading ischemia. UFF-PAM can provide the imaging speed, resolution, and FOV needed to capture the vasculature morphology and oxygenation changes during an SD wave event, which to the best of our knowledge has not been achieved previously by other photoacoustic imaging technologies.

## **CONCLUSION and DISCUSSION**

In conclusion, we have developed an innovative UFF-PAM system that has simultaneously achieved high imaging speed, large field of view, and high spatial resolution. By using SRS-based dual-wavelength excitation and water-immersible polygon-scanner, UFF-PAM can capture the hemodynamic changes in the brain, with a 3D frame rate of 2 Hz over an FOV of  $11 \times 10 \times 1.5$  mm<sup>3</sup>, and a lateral resolution of 10 μm. The maximum 2D frame rate is more than 2 kHz over an 11 mm scanning range. To our best knowledge, UFF-PAM is currently the fastest functional PAM system, while our previously reported polygon PAM system was not capable of functional imaging [23]. An automatic imaging registration method and a deep learning based upsampling approach were developed to mitigate the inter-facet misalignment and the spatial undersampling.

When fast scanning is needed, a rotating polygon mirror is a popular choice due to its simplicity and high speed. There is no need for an oscillating component or a complex driving system. Unlike the commonly used galvo scanners, which allow flexible control of the beam position, the maximum scanning angle of the polygon scanner is determined by the number of facets and the incoming beam size. We developed a water-immersed polygon scanner and calibrated for various misalignment between different facets. However, in our current setup, the need for water immersion limits the maximum imaging speed and image quality, mostly due to the water's damping force and resistance. Polygon scanners operating in air are more stable and faster than

the water-immersible polygon scanners. Cylindrically focused ultrasound transducers coupled with fast optical scanning can be utilized to mitigate the need for scanning the acoustic beam.

Due to the fast imaging speed, limited laser pulse rate and the laser safety concern, UFF-PAM has severe undersampling along the fast-scanning axis. This undersampling cannot be addressed by using interpolation methods, which can introduce image blurring and aliasing artifacts, such as jagged vessel boundaries, and cannot effectively improve the resolution. To tackle this problem, we applied a deep learning model modified from the Fully Dense U-net (FD U-net), which builds upon the popular U-Net architecture using Dense blocks and robust regularization in the form of 2D spatial dropout. This spatial dropout randomly drops entire convolutional filters during model training, thereby ensuring that both feature redundancy and robustness are incorporated into our model. This model was trained to reconstruct undersampled PAM images of *in vivo* mouse brain vasculature with as few as 2% of the original pixels [25]. In addition, because our model learns to restore vessel continuity, it can also remove any remaining facet misalignment.

Using UFF-PAM, we can image fast hemodynamic pathophysiology in the mouse brain on the global and local level, and can investigate oxygen delivery versus extraction/consumption dynamics based on the hemoglobin oxygenation measurement. As our hypoxia results demonstrate, UFF-PAM can make a unique contribution to the understanding of arterial oxygen content induced changes in cerebral blood flow (CBF) regulation. While the mechanisms underlying the influence of hypoxia upon CBF are complex and involve interactions of many physiological, metabolic, and biochemical processes, there is emerging evidence showing that deoxy-hemoglobin is the primary regulator of CBF [29]. We have shown that during hypoxic conditions arterial and venous  $sO_2$  is affected differently, more pronounced in veins, as OEF increases. Therefore UFF-PAM not only allows to observe global hemoglobin oxygenation kinetics as other technologies, but also to differentiate between arteries and veins, which reflect oxygen delivery versus oxygen extraction or consumption. Applying our system on a well-known hypoxia model [29], our results support the important role of  $sO_2$  in the regulation of blood flow. Next, we investigated the cerebral response, with particular focus on the microcirculation, to critical hypotension induced by the systemic vasodilator SNP. SNP has been widely used in clinical practice as a vasodilator (*e.g.*, during hypertensive crisis) for more than 50 years [49-53]. However, studies of SNP effects on the brain vasculature have remained elusive [34, 36]. Although

our previous study reported the brain hemodynamic response to SNP *in vivo* [54], and found vasodilation and decreased oxygenation after SNP application, we were not able to capture the functional dynamics in different types of vessels, due to the low imaging speed (3 min per image) and small FOV ( $3 \times 3 \text{ mm}^2$ ). By contrast, UFF-PAM was capable of visualizing the rapid hemodynamic response to SNP-induced substantial hypotension. Our results have demonstrated the rapid vasodilation in large vessels and yet constriction in microvessels, further underlining the necessity for high resolution imaging of blood oxygenation. Lastly, our spreading ischemia experiments demonstrated that prolonged cerebral ischemia could trigger microvascular constriction waves, resulting in increased oxygen extraction. These microvascular constriction waves follow spreading depolarization events in the brain [40], which have been proved to contribute to secondary lesion enlargement. The high resolution and large FOV of UFF-PAM allowed monitoring the local initiation of the SD, as well as tracking the propagation pattern and vasoconstriction over the entire event across the whole cortex. UFF-PAM can potentially be used for the stroke research community to discern stroke core, penumbra, as well as expansion of the penumbra in real time, and assess neuroprotective therapies in future studies.

In summary, we have developed a high-speed wide-field functional PAM technology that may provide a powerful tool for studying cerebral hemodynamics of the mouse brain in a wide range of pathological and physiological models.

## **Methods**

### **Animal preparation**

All animal procedures were reviewed and approved by the Institutional Animal Care and Use Committee (IACUC) of Duke University (Protocol No: A009-20-01), and were conducted in accordance with National Institutes of Health guidelines. C57BL/6 mice (3-5 months old; weight, 20-30 gram) were used in all the *in vivo* experiments. The pulse energy at the surface of the mouse brain was ~200 nJ per wavelength. A 3D-printed nose cone securely mounted the mouse head. We kept the mouse under anesthesia with 1.5% v/v isoflurane throughout the imaging experiment, and the body temperature was maintained at 37 °C using a heating pad.

### **The 12-facet polygon scanner**

The 12-facet polygon scanner was fabricated from aluminum, and single-point diamond machining technology was applied to create the optical facets. Its clear aperture is 5 mm along the fast-scanning axis and 9 mm along the slow scanning axis. The polygon diameter is 21 mm, and light reflection on each facet is >88% at 532 nm. A water-immersible DC electric motor (M1N10FB11G, Minebea Mitsumi) enables the polygon to operate smoothly at speeds ranging from a few rpm (revolutions per minute) to greater than 10,000 rpm, which corresponds to more than 2 kHz line scanning rate for the 12-facet polygon (**Supplementary Video 1**).

### **The ring-shaped ultrasound transducer**

A ring-shaped, focused ultrasound transducer with a central frequency at 40 MHz was designed and fabricated in the lab. First, a piezoelectric transducer modeling software (PiezoCAD) based on Krimboltz, Leedom, and Mattaei (KLM) equivalent circuit model was employed to optimize the design of the transducer. According to the optimized parameters, a lithium niobate (LNO) plate (70 μm thickness) (Boston Piezo-Optics) was selected as the core piezoelectric layer. Next, a 10-μm-thick first matching layer made of silver loaded epoxy and a 3-mm-thick backing material (conductive silver paste, E-solder 3022, Von Roll Isola) were deposited onto the front and back sides of the LNO plate, respectively. The matched and backed acoustic stack was then machined into a ring and inserted and fixed into a brass housing with a height of 4 mm. A central aperture with a diameter of 3 mm was drilled to deliver light, enabling co-axial alignment of optical excitation and acoustic detection for maximum detection sensitivity. The outer diameter of the

transducer element is 6 mm. The gap was filled with epoxy resin (EPO-TEK 301, Epoxy Technology) and one lead wire was connected through the backing. After that, the transducer was pressed by a metal ball to form a focal length of 8 mm. A Cr/Au (50/100 nm) electrode was sputtered across the first matching layer and the brass housing to form a common ground connection. Finally, a 10- $\mu$ m-thick parylene layer was deposited onto the entire external surface of the device as the second matching layer to compensate for the acoustic impedance mismatch with water.

### **The start of scan (SOS) system**

We used the PA excitation light as the laser source and an optical fiber as the receiver to build the lab-made SOS system. A multimode fiber (M45L02, Thorlabs) was mounted beneath the ultrasound transducer to receive the laser light. When the polygon rotated to the starting edge of each facet, the steered laser beam landed on the tip of the multimode fiber. A high-speed photodiode (PDA36A2, Thorlabs) was used to detect the received light by the fiber, and converted it into a SOS trigger signal. The lab-made SOS system was compact with high accuracy. The SOS signal triggered the FPGA card which synchronized the two PA lasers and the DAQ card.

### **The Raman-shifter based dual-wavelength laser system**

The 6.5-meter polarization-maintaining single-mode fiber (HB450-SC, FIBERCORE) was positioned with a fiber alignment stage (561D-XYZ, Newport) and a bare fiber chuck (FPH-S, Newport). The fiber tip was fixed with a universal bare fiber terminator (BFT1, Thorlabs), and the output beam from the fiber was collimated by an achromatic fiber port (PAF2A-A10A, Thorlabs). We measured the optical spectrum of the output laser after the achromatic fiber port with an optical spectrometer (CCS175, Thorlabs). The critical power and the maximum power of the  $n^{\text{th}}$ -order Raman amplification in a silica fiber are given by [55]

$$P_N^{Cr} \approx 16 \times N \times A_{eff} / (g_R L_{eff}) \quad (1)$$

$$P_N^{Max} \approx 30 \times N \times A_{eff2} / (g_{R2} L_{eff2}) \exp(-\alpha L) \quad (2)$$

where  $P_N^{Cr}$  and  $P_N^{Max}$  are the necessary pumping power to reach the Raman threshold and the maximum output power of the  $n^{\text{th}}$ -order Stokes, respectively. The  $A_{eff}$  and the  $A_{eff2}$  are the effective mode area of the pump light in the fiber for the first and second stokes waves, respectively.  $g_R$  and  $g_{R2}$  are the Raman gain coefficients.  $L_{eff}$  and  $L_{eff2}$  are the effective lengths for first and second stokes waves, respectively.  $L$  is the fiber length, and  $\alpha$  is the fiber attenuation coefficient. The maximum Raman scattering efficiency of the single-mode fiber occurs at a frequency shift of  $\sim 13.2$  THz, corresponding to 545 nm for the first stoke and 558 nm for the second stoke. We chose the second stoke light for functional imaging because of the larger difference in the optical absorption between oxy- and deoxy-hemoglobin. The 558 nm light pulse energy after the dichroic mirror (DMSP550, Thorlabs) was  $\sim 500$  nJ.

### Inter-facet image registration

Image registration is used to find an optimal spatial transform that maps pixels from the template image  $I_1$  by the reference facet to the corresponding pixels in the target image  $I_2$  by the misaligned facet,

$$I_1 = [x \ y]; \quad I_2 = [x' \ y']; \quad (3)$$

The target image  $I_2$  has a distortion relative to the template image  $I_1$  that can be described by a 2D geometric transformation  $T$ ,

$$[x' \ y' \ 1] = [x \ y \ 1] \times T \quad (4)$$

$$T = \begin{bmatrix} s_c & -s_s & 0 \\ s_s & s_c & 0 \\ t_x & t_y & 1 \end{bmatrix} \quad (5)$$

where  $T$  is a 3-by-3 matrix that depends on four parameters.

$$s_c = scale \times \cos (angle) \quad (6)$$

$$s_s = scale \times \sin (angle) \quad (7)$$

where ‘scale’ is the scaling factor, ‘angle’ is the rotation angle,  $t_x$  is the  $x$ -translation, and  $t_y$  is the  $y$ -translation. We chose the image from one facet as the template (reference) image, and the other eleven images were used as the target images. After extracting the corresponding geometric transformation  $T$ , we performed the inverse transform  $T^{-1}$  on the eleven target images. A simple automated image registration method was used to address the misalignment between the twelve facets. There were five steps in the registration process.

Step 1. We extracted every single facet image from the entire volume scan. We chose the first facet image as the fixed image known as  $I_1$  and the images from the other eleven facets as the moving images known as  $I_2$ . The adjacent B-scans from every single-facet image were aligned in the raw data.

Step 2. We used the function ‘imregtform’ in MATLAB to find the geometric transformations that mapped the images to be registered (moving) to the reference image (fixed). A ‘similarity’ model was used, which included translation, scaling, and rotation.

Step 3. We modified the geometric transformation and added  $y$ -translation, since there was  $y$ -axis shift between each facet.

$$t_y = t_{y'} - (i - 1)/12 \quad (8)$$

where  $t_{y'}$  is the  $y$ -translation calculated from the ‘imregtform’,  $i$  is the  $i$ th facet, and  $t_y$  is the modified  $y$ -translation.

Step 4. We performed the transformation by using the ‘imwarp’ function, which used the geometric transformation to map coordinates in the output image to the corresponding coordinates in the input image (inverse mapping).

Step 5. We interleaved lines from each facet into one final composite image.

### **Deep learning model for image upsampling**

As described in our previous work [25], we tested various deep learning model architectures, including U-net and some variations on U-net, and found a modified FD U-net performed best at the task of upsampling PAM images (see **Supplementary Fig. 4a** for model depiction). The

original FD U-net improved upon the traditional U-net architecture by replacing the typical convolutional blocks with Dense blocks – which had previously been shown to improve the performance of deeper convolutional neural networks (see **Supplementary Fig. 4b** for an in-depth depiction of Dense blocks). We then further modified this FD U-net archetype by replacing RELU activation functions with ELU (which also helps improve the performance of deeper networks), replacing max pooling with strided convolutions (to allow for learned downsampling within the network), and by adding spatial dropout ( $p=0.05$ ) to regularize the network and improve robustness. This last modification, in addition to the extensive image augmentation used during training, are especially important in this work, as a model originally trained on traditional PAM images was able to successfully extrapolate to 12-facet polygon PAM images. Due to updates in the deep learning framework used (*i.e.*, Tensorflow) we were able to discard the “model patchwork algorithm” of our previous work – which processed 128 by 128 pixel crops of larger images – in favor of applying our fully convolutional neural network on entire 12-facet images at a time. The general deep learning image processing framework is depicted in **Supplementary Fig. 5** and went as follows:

Step 1. We saved the mins and maxes of the facet-aligned polygon images and normalized the images to between [0, 1]

Step 2. We performed an initial upsampling to change the images to their final upsampled shape by adding zero pixels to represent where undersampling occurred (see **Supplementary Fig. 5** *Zerofill Image*).

Step 3. We fed these images as input into our deep learning model. Although the model was originally trained on  $128 \times 128$  pixel crops, larger images can now be used as input during inference (as our neural network is fully convolutional).

Step 4. We then renormalized each of the images using the saved mins and maxes, to allow for extraction of functional information (such as  $sO_2$ )

### **Transcranial brain window**

To optimize the *in vivo* performance, we developed a whole-cortex transcranial brain window that was both optically and acoustically transparent. The window was trapezoidal-shaped, with a 9 mm by 10 mm frame size and a useable opening of 8 mm by 7.5 mm. To avoid compressing brain

tissue and damaging blood vessels, the window frame had a curved surface that followed the mouse skull's natural curvature. The window frame was 3D printed using PLA. The window opening was sealed with PVC membrane (10  $\mu\text{m}$  thick) that was both optically and acoustically transparent.

To install the brain window, mice were anesthetized by 100 mg/kg ketamine and 10 mg/kg xylazine. After mounting the mouse head into a stereotactic frame, mice were shaved, and the head surface was cleaned using iodine and alcohol. After midline skin incision, the skin was retracted to fully expose the skull from the olfactory tract area to the occipital area and laterally to the border of the temporal muscles. The skull was kept wet using saline, and two coronal lines at the level of AP  $-2$  mm and AP  $+4$  mm and two sagittal lines along the border of temporal muscles were drilled until the skull became moveable. Using bone wax to seal tiny bleeding sites, the skull was carefully lifted and removed. The transcranial window was then mounted on the skull and glued using Cyanoacrylate (BSI, Atascadero, CA). Next, the skin was glued along the side edges of the window frame. The mouse was returned to the home cage and treated with three days of 5 mg/kg carprofen via subcutaneous (s.c.) injection (Levafen injection, Patterson Veterinary) and seven days of 5 mg/kg enrofloxacin via s.c. injection (Sigma). After a recovery period of seven days, mice were ready for imaging.

### **Systemic hypoxia**

Mice were anesthetized with 1.5% isoflurane and kept on a heating pad to maintain body temperature at 37  $^{\circ}\text{C}$ . Systemic hypoxia was induced by decreasing the oxygen content of the inspiratory air from 21% to 3% via flowmeters. After normoxia baseline imaging for 6 minutes, we introduced hypoxia for 2 minutes and imaged the resultant physiological changes. We repeated the normoxia/hypoxia cycle for 3 times to test the stability of the system. We monitored the mice continuously over 30 minutes.

### **SNP application**

SNP solution (Somerset Pharma) was prepared in saline (concentration: 250  $\mu\text{g mL}^{-1}$ ) immediately before use, and kept in a dark environment at 4  $^{\circ}\text{C}$  to prevent deterioration. SNP (25 mg/kg) was injected via a femoral vein catheter (PE 10) over a 40 second period using a syringe pump. In a subset of mice, we also cannulated the femoral artery and measured systemic blood pressure and brain tissue oxygenation. For monitoring  $\text{ptO}_2$  in the cortex, we used an oxygen electrode (Clarke-

style, 25 micrometer tip diameter; Unisense, Picoammeter PA 2000, Arhus) over the observation period.

### **Cerebral ischemic stroke**

The left carotid artery was permanently ligated with a 6.0 suture, while the right carotid artery was clamped temporarily with a small vascular clip. After 9 minutes of dual carotid artery occlusion, the clamp on the right carotid artery was removed to allow restoration of blood flow and reperfusion.

### **PA data analysis**

We carry out quantitative data analyses based on the imaging results to evaluate cerebral hemodynamics and metabolism changes corresponding to physiological states (hypoxia challenge, SNP, and ischemic stroke). By using the lab-developed vessel segmentation method, we quantified the total vessel area, average  $sO_2$  (a threshold of 0.65 to distinguish arteries from veins), and averaged vessel diameter. A total of 6-8 arteries and 6-8 veins per mouse were analyzed, with vessels being randomly selected. The hemodynamic quantities were all quantified over the entire mouse brain. For all analyses, we calculated the percentage changes from their baseline values. We used paired *t*-tests, and all statistical data were presented with a standard error of the mean (SEM), with *p*-values of  $<0.05$  being considered significant.

### **Acknowledgements**

We thank Dr. Caroline Connor for editing the manuscript. This work was sponsored by National Institutes of Health (R01 EB028143, R01 NS111039, RF1 NS115581, R21 EB027304, R21EB027981, R43 CA243822, R43 CA239830, R44 HL138185); American Heart Association Collaborative Sciences Award (18CSA34080277); Chan Zuckerberg Initiative Grant on Deep Tissue Imaging 2020-226178 by Silicon Valley Community Foundation.

### **Author contributions**

J.Y conceived and directed the project. X.Z. set up the imaging system, performed all experiments, and analyzed the data. L.J. and Q.Z. manufactured the ultrasound transducer. Q.H contributed to the surgery of ischemic stroke. A.D. developed the deep learning model and processed the data. T.V. contributed to the LabVIEW controlling program. Q.R. contributed to the Raman shifter. X.P.

contributed to the data processing. H.S. performed the surgery on the brain window. U.H. contributed to SNP experiment and interpretation of the animal experiment results. All the authors discussed the results. X.Z., Q.H., J.L., A.D., U.H. and J.Y. wrote the manuscript.

### **Competing interests**

The authors declare no competing interests.

### **Additional information**

Supplementary information is available for this paper.

## References

1. Raichle, M.E. and M.A. Mintun, *Brain work and brain imaging*. Annu Rev Neurosci, 2006. **29**: p. 449-76.
2. Hillman, E.M., *Optical brain imaging in vivo: techniques and applications from animal to man*. J Biomed Opt, 2007. **12**(5): p. 051402.
3. Sakadzic, S., et al., *Two-photon high-resolution measurement of partial pressure of oxygen in cerebral vasculature and tissue*. Nat Methods, 2010. **7**(9): p. 755-9.
4. Hillman, E.M., et al., *Depth-resolved optical imaging and microscopy of vascular compartment dynamics during somatosensory stimulation*. Neuroimage, 2007. **35**(1): p. 89-104.
5. Errico, C., et al., *Ultrafast ultrasound localization microscopy for deep super-resolution vascular imaging*. Nature, 2015. **527**(7579): p. 499-502.
6. Yao, J. and L.V. Wang, *Photoacoustic Microscopy*. Laser Photon Rev, 2013. **7**(5).
7. Wang, L.V. and S. Hu, *Photoacoustic tomography: in vivo imaging from organelles to organs*. Science, 2012. **335**(6075): p. 1458-62.
8. Zhang, H.F., et al., *Imaging of hemoglobin oxygen saturation variations in single vessels in vivo using photoacoustic microscopy*. Applied Physics Letters, 2007. **90**(5).
9. Maslov, K., et al., *Optical-resolution photoacoustic microscopy for in vivo imaging of single capillaries*. Optics Letters, 2008. **33**(9): p. 929-931.
10. Xie, Z., et al., *Laser-scanning optical-resolution photoacoustic microscopy*. Optics Letters, 2009. **34**(12): p. 1771-1773.
11. Yuan, Y., S. Yang, and D. Xing, *Optical-resolution photoacoustic microscopy based on two-dimensional scanning galvanometer*. Applied Physics Letters, 2012. **100**(2).
12. Kim, J.Y., et al., *High-speed and high-SNR photoacoustic microscopy based on a galvanometer mirror in non-conducting liquid*. Sci Rep, 2016. **6**: p. 34803.
13. Yao, J., et al., *Wide-field fast-scanning photoacoustic microscopy based on a water-immersible MEMS scanning mirror*. J Biomed Opt, 2012. **17**(8): p. 080505-1.
14. Kim, J.Y., et al., *Fast optical-resolution photoacoustic microscopy using a 2-axis water-proofing MEMS scanner*. Sci Rep, 2015. **5**: p. 7932.
15. Yao, J., et al., *High-speed label-free functional photoacoustic microscopy of mouse brain in action*. Nat Methods, 2015. **12**(5): p. 407-10.
16. Chen, Q., et al., *Ultracompact high-resolution photoacoustic microscopy*. Opt Lett, 2018. **43**(7): p. 1615-1618.
17. Lin, L., et al., *Handheld optical-resolution photoacoustic microscopy*. J Biomed Opt, 2017. **22**(4): p. 41002.
18. Jin, T., et al., *Portable optical resolution photoacoustic microscopy (pORPAM) for human oral imaging*. Opt Lett, 2017. **42**(21): p. 4434-4437.
19. Jin, T., et al., *Portable optical-resolution photoacoustic microscopy for volumetric imaging of multiscale organisms*. J Biophotonics, 2018. **11**(4): p. e201700250.
20. Lin, Y.C., et al., *A compact and portable laser radioactive decontamination system using passive Q-switched fiber laser and polygon scanner*. Appl Radiat Isot, 2019. **153**: p. 108835.
21. Li, Y.X., et al., *Flexible polygon-mirror based laser scanning microscope platform for multiphoton in-vivo imaging*. J Biophotonics, 2017. **10**(11): p. 1526-1537.

22. Ji, Y.-Y., B.H. So, and D.Y. Kim, *High-speed time-domain characterization method for polygon scanners*. Measurement, 2019. **135**: p. 278-286.
23. Lan, B., et al., *High-speed widefield photoacoustic microscopy of small-animal hemodynamics*. Biomed Opt Express, 2018. **9**(10): p. 4689-4701.
24. Chen, J., et al., *Wide-field polygon-scanning photoacoustic microscopy of oxygen saturation at 1-MHz A-line rate*. Photoacoustics, 2020. **20**: p. 100195.
25. DiSpirito, A., et al., *Reconstructing Undersampled Photoacoustic Microscopy Images Using Deep Learning*. IEEE Trans Med Imaging, 2021. **40**(2): p. 562-570.
26. Ainslie, P.N. and S. Ogoh, *Regulation of cerebral blood flow in mammals during chronic hypoxia: a matter of balance*. Exp Physiol, 2010. **95**(2): p. 251-62.
27. Bain, A.R. and P.N. Ainslie, *On the limits of cerebral oxygen extraction*. J Physiol, 2014. **592**(14): p. 2917-8.
28. Willie, C.K., et al., *Integrative regulation of human brain blood flow*. J Physiol, 2014. **592**(5): p. 841-59.
29. Hoiland, R.L., et al., *Hypoxemia, oxygen content, and the regulation of cerebral blood flow*. Am J Physiol Regul Integr Comp Physiol, 2016. **310**(5): p. R398-413.
30. Lewis, N.C.S., et al., *Effect of acute hypoxia on regional cerebral blood flow: effect of sympathetic nerve activity*. Journal of applied physiology (Bethesda, Md. : 1985), 2014. **116**(9): p. 1189-1196.
31. Hoiland, R.L., et al., *Adenosine receptor-dependent signaling is not obligatory for normobaric and hypobaric hypoxia-induced cerebral vasodilation in humans*. Journal of applied physiology (Bethesda, Md. : 1985), 2017. **122**(4): p. 795-808.
32. Morris, L.E., et al., *Cerebrovascular and ventilatory responses to acute normobaric hypoxia in girls and women*. Physiol Rep, 2017. **5**(15).
33. Ivankovich, A.D., D.J. Miletich, and J.H. Tinker, *Sodium nitroprusside: metabolism and general considerations*. Int Anesthesiol Clin, 1978. **16**(2): p. 1-29.
34. Stånge, K., M. Lagerkranser, and A. Sollevi, *Nitroprusside-induced hypotension and cerebrovascular autoregulation in the anesthetized pig*. Anesth Analg, 1991. **73**(6): p. 745-52.
35. Hoffman, W.E., et al., *Sodium nitroprusside compared with isoflurane-induced hypotension: the effects on brain oxygenation and arteriovenous shunting*. Anesth Analg, 2001. **93**(1): p. 166-70.
36. Olesen, N.D., M. Fischer, and N.H. Secher, *Sodium nitroprusside dilates cerebral vessels and enhances internal carotid artery flow in young men*. J Physiol, 2018. **596**(17): p. 3967-3976.
37. Adnot, S., et al., *Effects of sodium-nitroprusside and urapidil on gas exchange and ventilation-perfusion relationships in patients with congestive heart failure*. European Respiratory Journal, 1991. **4**(1): p. 69-75.
38. Wildsmith, J., G. Drummond, and W. MacRae, *Blood-gas changes during induced hypotension with sodium nitroprusside*. BJA: British Journal of Anaesthesia, 1975. **47**(11): p. 1205-1211.
39. Sugimoto, K., et al., *Peri-Infarct Hot-Zones Have Higher Susceptibility to Optogenetic Functional Activation-Induced Spreading Depolarizations*. Stroke, 2020. **51**(8): p. 2526-2535.
40. Ayata, C. and M. Lauritzen, *Spreading Depression, Spreading Depolarizations, and the Cerebral Vasculature*. Physiol Rev, 2015. **95**(3): p. 953-93.

41. Shin, H.K., et al., *Vasoconstrictive neurovascular coupling during focal ischemic depolarizations*. J Cereb Blood Flow Metab, 2006. **26**(8): p. 1018-30.
42. Strong, A.J., et al., *Peri-infarct depolarizations lead to loss of perfusion in ischaemic gyrencephalic cerebral cortex*. Brain, 2007. **130**(Pt 4): p. 995-1008.
43. Hartings, J.A., et al., *The continuum of spreading depolarizations in acute cortical lesion development: Examining Leao's legacy*. J Cereb Blood Flow Metab, 2017. **37**(5): p. 1571-1594.
44. Dreier, J.P., *The role of spreading depression, spreading depolarization and spreading ischemia in neurological disease*. Nature Medicine, 2011. **17**(4): p. 439-447.
45. von Bornstadt, D., et al., *Supply-demand mismatch transients in susceptible peri-infarct hot zones explain the origins of spreading injury depolarizations*. Neuron, 2015. **85**(5): p. 1117-31.
46. Mestre, H., et al., *Cerebrospinal fluid influx drives acute ischemic tissue swelling*. Science, 2020. **367**(6483).
47. Hoffmann, U., et al., *Glucose modulation of spreading depression susceptibility*. J Cereb Blood Flow Metab, 2013. **33**(2): p. 191-5.
48. Hoffmann, U., et al., *Increased glucose availability does not restore prolonged spreading depression durations in hypotensive rats without brain injury*. Exp Neurol, 2012. **238**(2): p. 130-2.
49. Hottinger, D.G., et al., *Sodium nitroprusside in 2014: A clinical concepts review*. Journal of anaesthesiology, clinical pharmacology, 2014. **30**(4): p. 462-471.
50. Friederich, J.A. and J.F. Butterworth, *Sodium Nitroprusside: Twenty Years and Counting*. Anesthesia & Analgesia, 1995. **81**(1).
51. Mullens, W., et al., *Sodium nitroprusside for advanced low-output heart failure*. J Am Coll Cardiol, 2008. **52**(3): p. 200-7.
52. Costard-Jäckle, A. and B. Fowler Michael, *Influence of preoperative pulmonary artery pressure on mortality after heart transplantation: Testing of potential reversibility of pulmonary hypertension with nitroprusside is useful in defining a high risk group*. Journal of the American College of Cardiology, 1992. **19**(1): p. 48-54.
53. Kowaluk, E.A., P. Seth, and H.L. Fung, *Metabolic activation of sodium nitroprusside to nitric oxide in vascular smooth muscle*. Journal of Pharmacology and Experimental Therapeutics, 1992. **262**(3): p. 916.
54. Zhang, D., et al., *Photoacoustic imaging of in vivo hemodynamic responses to sodium nitroprusside*. J Biophotonics, 2021: p. e202000478.
55. de la Cruz-May, L., et al., *Raman threshold for nth-order cascade Raman amplification*. Optical Fiber Technology, 2011. **17**(3): p. 214-217.

## Figures and captions

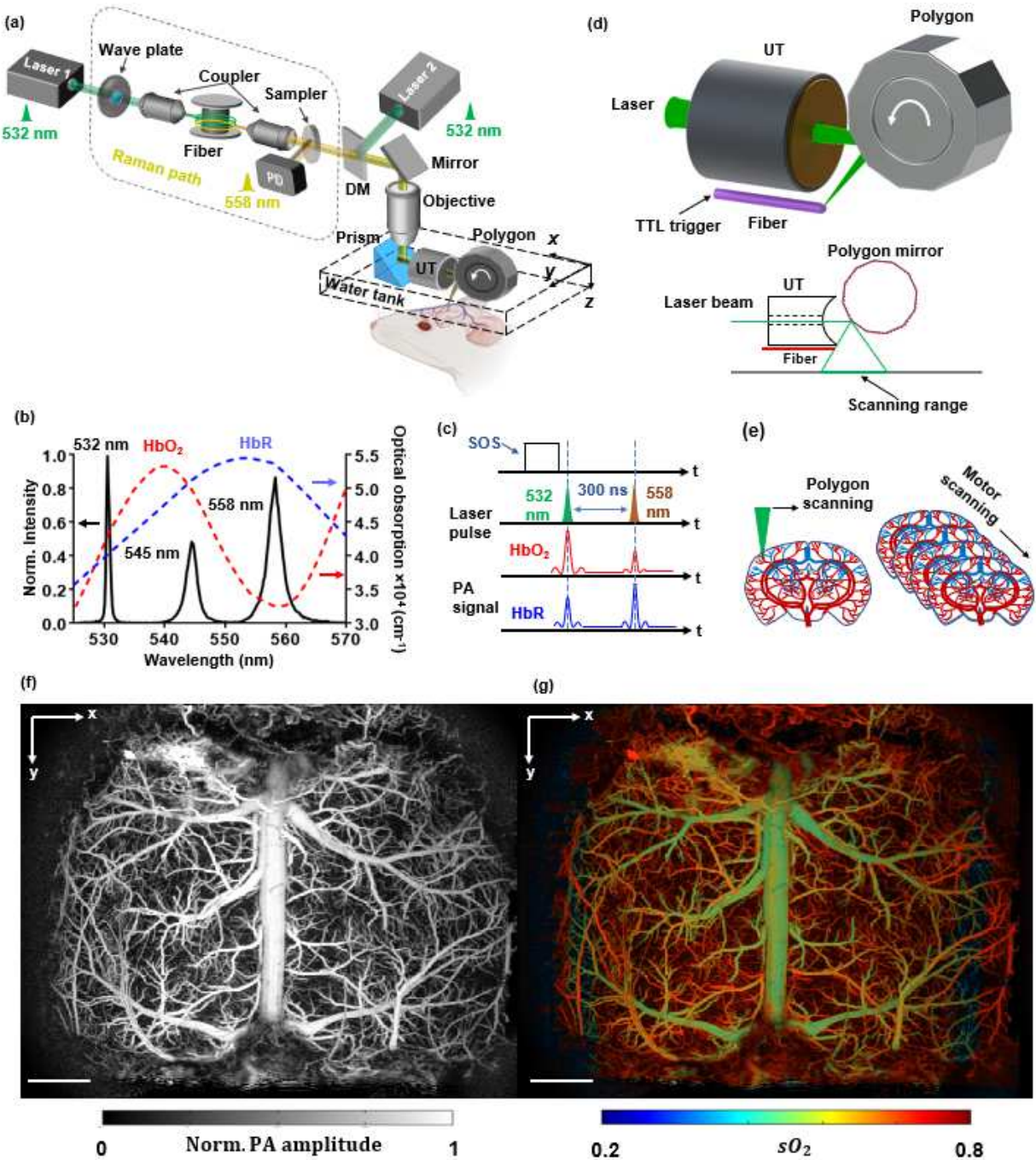


**Figure. 1** Ultrafast functional photoacoustic microscopy (UFF-PAM) with high imaging speed and wide field of view. (a) Schematic of the UFF-PAM system. The 532 nm light path and the 558 nm Raman path are combined for functional imaging. DM, dichroic mirror; PD,

photodiode; UT, ultrasound transducer. (b) The optical spectrum of the Raman path output, and the absorption spectra of oxy-hemoglobin (HbO<sub>2</sub>) and deoxy-hemoglobin (HbR). (c) The dual-wavelength excitation sequence and the resultant PA signals from HbO<sub>2</sub> and HbR. (d) The close-up schematic of the ultrasound transducer, the polygon scanner, the start of scan (SOS) detection, and the scanning range. (f) A representative *x-y* maximum amplitude projection (MAP) image of a mouse brain vasculature over the entire cortex, acquired by UFF-PAM at 532 nm. (g) The oxygen saturation of hemoglobin (sO<sub>2</sub>) map of the same mouse brain, acquired with dual-wavelength measurements at 532 nm and 558 nm. Scale bar in (f-g), 1 mm.

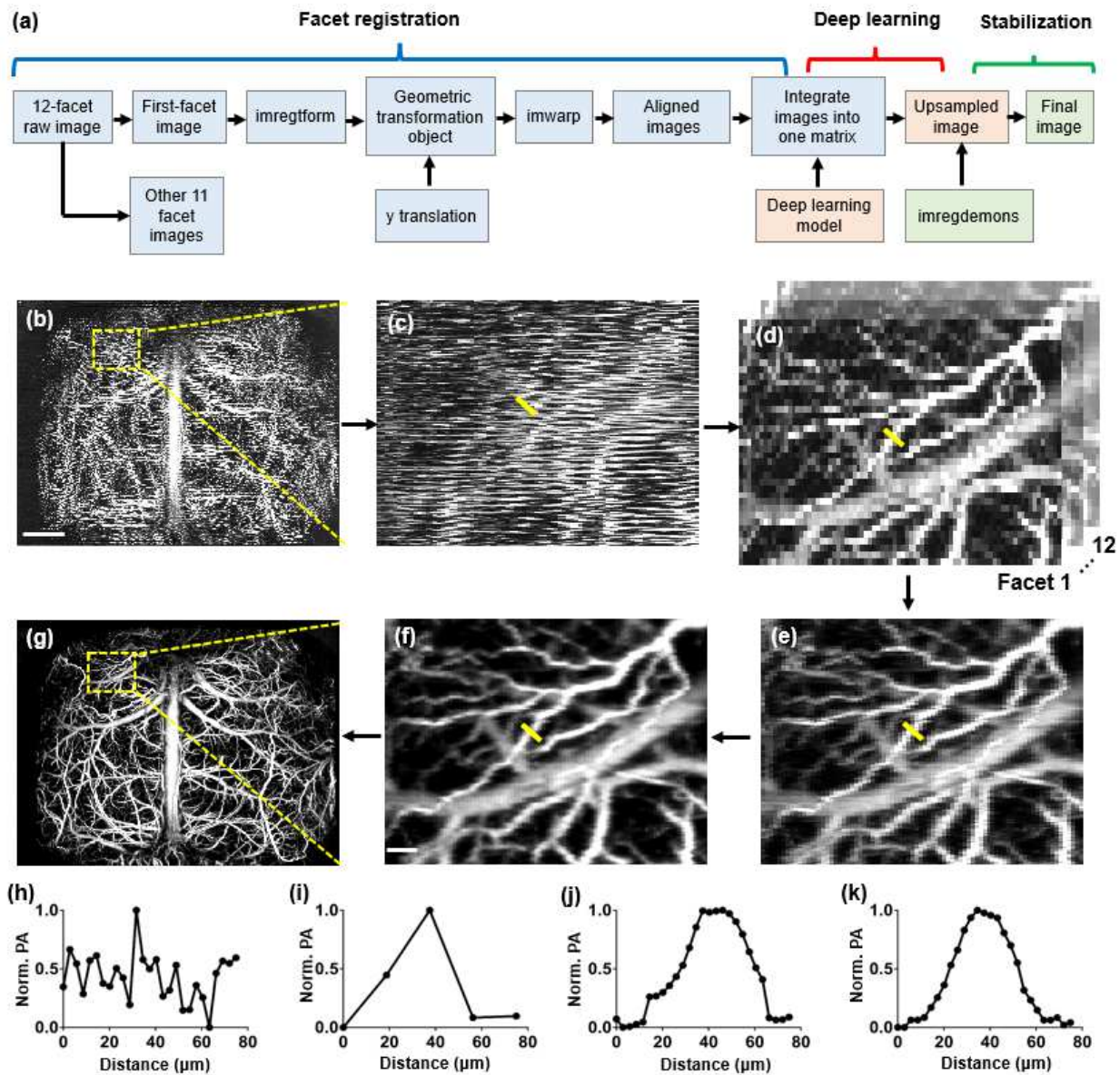


**Figure 2. Image registration and deep learning based upsampling in UFF-PAM.** (a) The flowchart of the imaging process in UFF-PAM, including the facet registration, deep learning based upsampling, and frame stabilization. (b) The misaligned and undersampled PA image of the whole cortex, generated by all 12-facets. (c) Close-up image of the dashed box region in (b), showing the misalignment of each facet. (d) Close-up images generated by each single facet. (e) Close-up PA image after facet alignment. (f) Close-up PA image generated by deep learning based upsampling. (g) The whole-cortex image improved by facet alignment and deep learning

upsampling. (h-k) The intensity profiles of the representative vessel marked by the yellow lines in (c-f), respectively. Scale bar in (b) and (g), 1 mm. Scale bar in (c-f), 100  $\mu\text{m}$ .

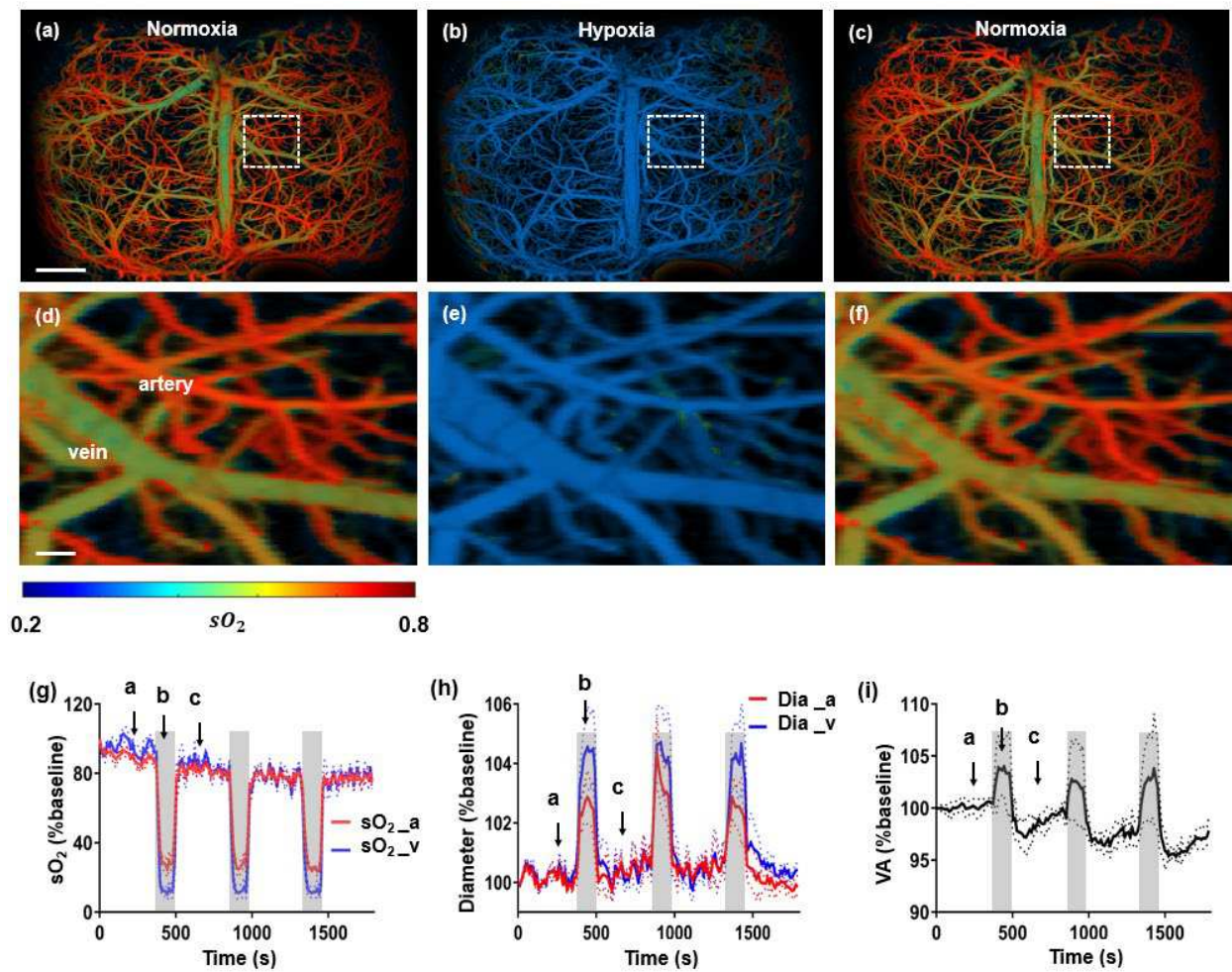


**Figure 3. UFF-PAM of brain hemodynamics under hypoxia.** (a, b, c) sO<sub>2</sub> images of the entire mouse cortex under a cycle of normoxia, hypoxia, and then returned to normoxia. (d, e, f) Close-up images of the dashed box regions in (a-c). (g) The averaged sO<sub>2</sub> changes in arteries (sO<sub>2</sub>\_a) and veins (sO<sub>2</sub>\_v). The grey areas indicate the hypoxia challenges. The arrows represent the time points corresponding to (a-c). (h) The diameter changes of the marked artery and vein in (d). (i) Vessel area (VA) change of the whole cortex. N=4. The data in (g-i) are shown as mean±sem. Scale bar, 1 mm in (a-c), 100 μm in (d-f).

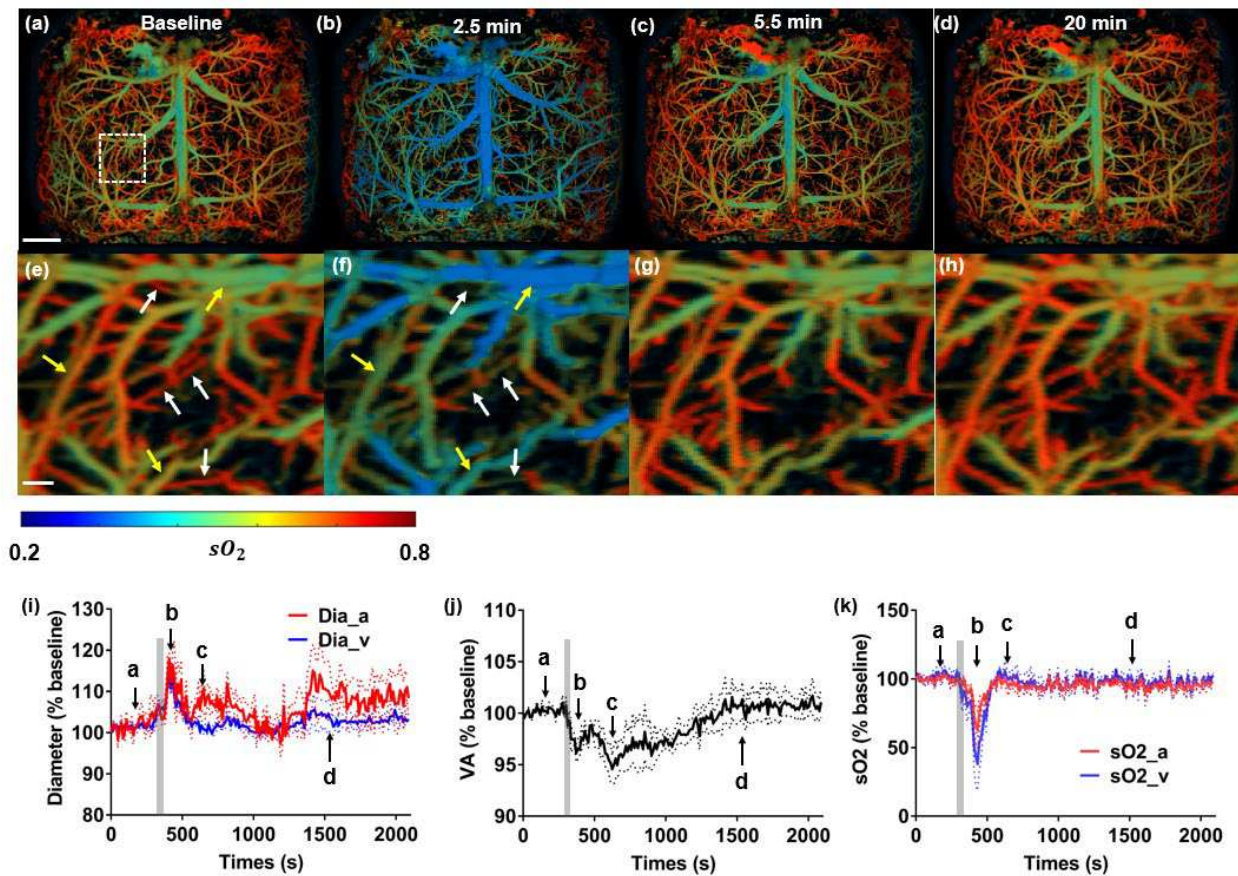


**Figure 4. UFF-PAM of brain hemodynamics in response to SNP.** (a-d) sO<sub>2</sub> images of the entire cortex of the mouse brain at baseline, as well as 2.5, 5.5, and 20 min after SNP injection. (e-h) Close-up sO<sub>2</sub> images at the respective time points, as indicated by the white dotted box in (a). The yellow arrows point to the representative dilated vessels, and the white arrows point to the representative constricted microvessels. (i) The average diameter changes of arteries and veins. The grey area represents the duration of SNP injection. (j) Vessel area change of the whole cortex. (k) The average sO<sub>2</sub> change of arteries and veins. The arrows in (i-k) represent the time points corresponding to (a-d). N=3. The data in (i-k) are shown as mean±sem. Scale bar, 1mm for (a-d), and 100 μm for (e-h).

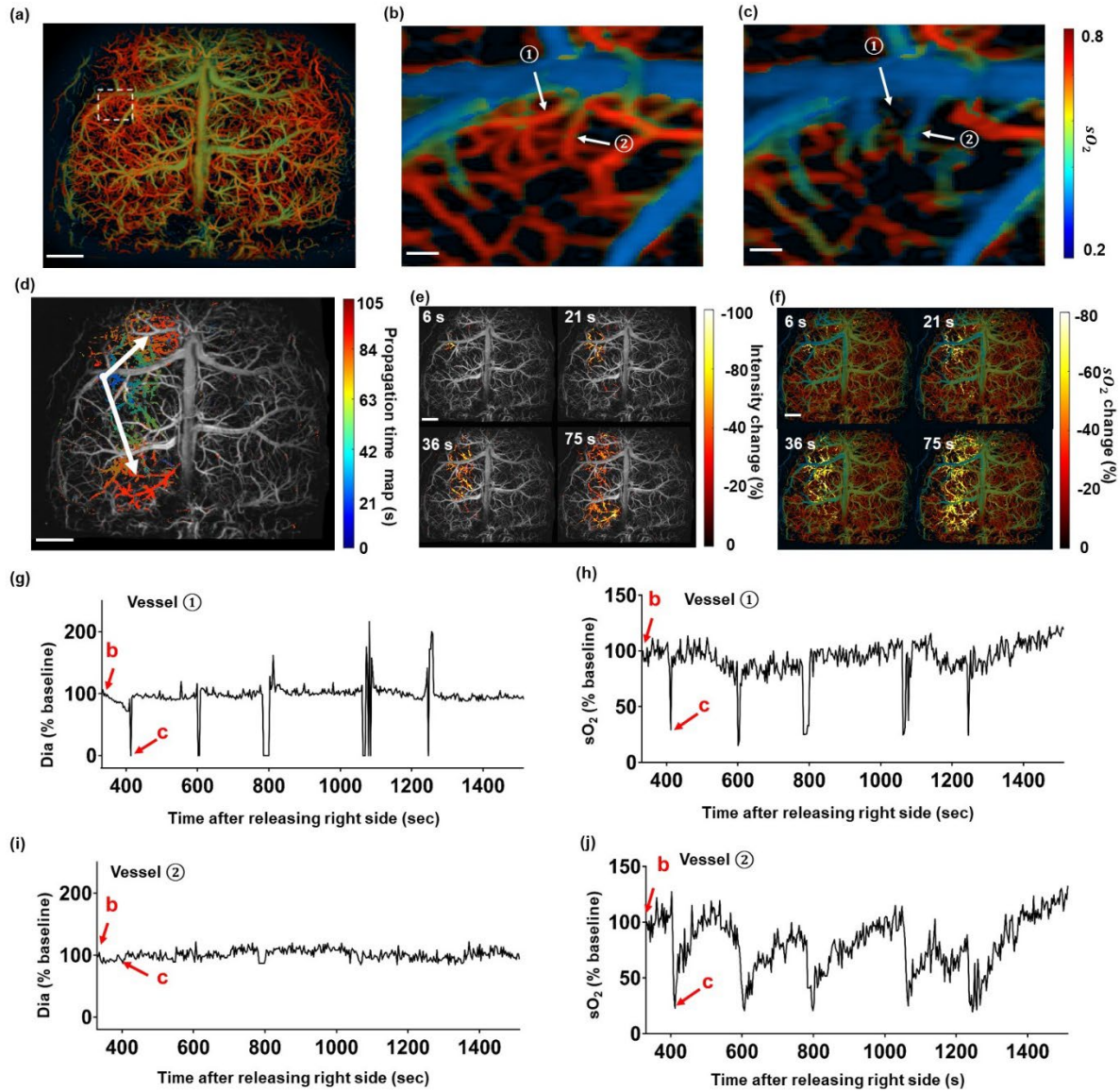


**Figure 5. UFF-PAM of the stroke-induced SD waves.** (a) sO<sub>2</sub> image of the whole cortex at baseline. (b, c) Close-up sO<sub>2</sub> images of the SD wave origin at 330s and 411s after releasing the right carotid artery, as indicated by the white dotted rectangle in (a). Two representative vessels ① and ② were selected for further analysis. (d) Propagation time map of a representative SD wave. Arrows represent the direction of SD wave. (e) The change in PA signal intensity during the SD wave propagation at 6s, 21s, 36s and 75s, respectively. (f) The change in sO<sub>2</sub> during the SD wave propagation. (g) The diameter change of vessel ① over a SD wave. (h) The sO<sub>2</sub> change of vessel ① over a SD wave. (i) The diameter change of vessel ②. (j) The sO<sub>2</sub> change of vessel ②. Scale bars, 1 mm for (a, d, e, f), 100 μm for (b, c).

## Supplementary Files

This is a list of supplementary files associated with this preprint. Click to download.

- [SupplementaryVideo1.mp4](#)
- [SupplementaryVideo2.mp4](#)
- [SupplementaryVideo3.mp4](#)
- [SupplementaryVideo4.mp4](#)
- [SupplementaryVideo5.mp4](#)
- [SupplementaryVideo6.mp4](#)
- [SupplementaryVideo7.mp4](#)
- [SupplementaryVideo8.mp4](#)
- [SupplementaryVideo9.mp4](#)
- [SupplementaryVideo10.mp4](#)
- [Supplementarydata.docx](#)